



Preparation and characterization of Cu modified BiYO₃ for carbon dioxide reduction to formic acid



Tongming Su^a, Hui Tian^a, Zuzeng Qin^{a,b,*}, Hongbing Ji^{a,b,*}

^a School of Chemistry and Chemical Engineering, Guangxi Key Laboratory of Petrochemical Resource Processing and Process Intensification Technology, Guangxi University, Nanning 530004, China

^b Department of Chemical Engineering, School of Chemistry & Chemical Engineering, Sun Yat-sen University, Guangzhou 510275, China

ARTICLE INFO

Article history:

Received 21 July 2016

Received in revised form

13 September 2016

Accepted 17 September 2016

Available online 19 September 2016

Keywords:

Copper doped

Bismuth yttrium oxide

Photocatalytic reduction

Carbon dioxide

Formic acid

ABSTRACT

Bismuth yttrium oxide (BiYO₃) photocatalysts doped with different Cu amounts were synthesized via a hydrothermal method, characterized and applied for the photocatalytic reduced CO₂ to formic acid under the visible light irradiation. The particle size of Cu/BiYO₃ was smaller than that of BiYO₃, and the surface area of BiYO₃ was increased from 6.75 m²/g to 18.64 m²/g when the Cu doping amount of was 2.0%. The FT-Raman results reveal the formation of oxygen vacancies after doping with Cu, which suppressed the charge recombination, and the electrochemical impedance spectroscopy (EIS) proved that the Cu/BiYO₃ has a better electronic transmission capacity. The HCOOH amount of photocatalytic reduction of CO₂ was 2.04 μmol/mL by using 2.0% Cu/BiYO₃ as photocatalyst, which was 2.2 times than that of BiYO₃. The highly improved performance of the 2.0% Cu/BiYO₃ can be ascribed to the increased surface area, increased light absorption, and efficient charge separation.

© 2016 Elsevier B.V. All rights reserved.

1. Introduction

Over the past decades, large emissions of carbon dioxide in the atmosphere from the combustion of fuels is one of the primary causes of global warming. It is indispensable to reduce our dependency on fossil fuels and meanwhile release the environmental burden. Therefore, tremendous research activities have been devoted to CO₂ capture, storage and utilization [1–4]. Furthermore, with the development of society, there has been a large increase in the utilization of fuels including coal, petroleum, and natural gas. Photocatalytic reduction of CO₂ into hydrocarbon fuels is considered to be a promising avenue to solve the problems relating to CO₂.

Photocatalyst used for photocatalytic reduce carbon dioxide with water to generate gaseous or liquid fuels such as CO, methane, methanol, and formic acid have been widely studied, such as Cu-TiO₂/ZSM-5 [5], Ag/C₃N₄ [6], Zn₂GeO₄ [7], Cu₂O/SiC [8]. TiO₂ is among the most studied photocatalyst due to its excellent stability, easy operation, low cost, and high catalytic properties. However, the recycling difficulties and the fast recombination of charge carrier limit the photocatalytic activity of TiO₂ particles. In addition,

the wide band gap (3.2 eV) of TiO₂ result in that it can make use of only 3–4% of the solar energy that reaches the earth [9]. Therefore, visible-light-driven photocatalyst should be developed in order to enhance the utilization of the sunlight.

The bismuth-containing semiconductor photocatalyst has good visible absorption performance and high photocatalytic activity because the valence band of Bi-based oxide semiconductors consist of Bi 6s and O 2p hybrid orbitals [10], which makes it have a relatively steep absorption edge in the visible range. However, there are still some drawbacks restricting its practical application, such as the limited region of visible-light photo-response and quick recombination of the photo-generated electron-hole pairs. Therefore, numerous studies have been devoted to develop visible light driven Bi-based oxide semiconductors by semiconductor composite [11], nonmetal ion doping [12], metal ion doping [13] and co doping modification [14]. A large number of studies show that metal ions doped into photocatalyst can significantly affect the production, transfer and recombination of photo-generated electrons and holes on the surface of photocatalyst [15–17]. The transition metal ions doped into photocatalyst may change the electronic distribution of the system, or change the crystal crystallinity, as a result, it may be used as photoinduced electron-hole pairs trap to increase the quantum efficiency of the heterogeneous photocatalytic property by altering the electron-hole pair recombination rate and promoting the interfacial charge transfer rates of

* Corresponding authors at: School of Chemistry and Chemical Engineering, Guangxi University, Nanning 530004, China.

E-mail addresses: qinzuzeng@gmail.com (Z. Qin), jihb@mail.sysu.edu.cn (H. Ji).

photo-generated carriers [18,19]. Research on the metal ion doped Bi-based oxide semiconductors, such as Er/BiOBr [20], Ag/Bi₂WO₆ [21], Y/Bi₂WO₆ [22], Cu/BiVO₄ [23,24], and La/Bi₂Ti₂O₇ [25] was studied. Copper is considered to be one of the most suitable doping elements, because it narrows the band gap of photocatalyst, increases the surface area and suppresses the charge recombination [26,27].

Based on our previous research on the BiYO₃ for photocatalytic degraded methyl orange [28] and photocatalytic reduction of CO₂ [29], BiYO₃ photocatalyst doped with 0.5 to 3.0% Cu were prepared via a hydrothermal method, and the effects of the Cu doping amounts on the structure of the BiYO₃ and photocatalytic reduction of CO₂ to formic acid under visible-light irradiation were studied in this work.

2. Experimental

2.1. Preparation of photocatalyst

BiYO₃ photocatalysts doped with different amount of Cu were prepared by a hydrothermal method [29]. 0.5 mol/L of Bi(NO₃)₃ aqueous solution and 0.5 mol/L of Y(NO₃)₃ aqueous solution were mixed evenly. Subsequently, 4.0 mol/L NH₄OH was added into the above mixture under stirring at 100 r/min to adjust the pH value to 8.0. After that, 0.5%, 1.0%, 2.0%, 3.0% (mole fraction) Cu(NO₃)₂ were added into the mixture and stirred at room temperature for 0.5 h, the mixture was transferred into a Teflon-lined stainless sealed autoclave and heated at 180 °C for 12 h. After natural cooling, the reactant was vacuum filtrated and washed with deionized water, and then dried at 90 °C for 10 h and calcined at 700 °C for 2 h to obtain the Cu/BiYO₃ with different Cu amounts (marked to 0.5% Cu/BiYO₃, 1.0% Cu/BiYO₃, 2.0% Cu/BiYO₃, and 3.0% Cu/BiYO₃). For comparison, the BiYO₃ photocatalyst was prepared by the same method as described above without adding the Cu(NO₃)₂.

2.2. Photocatalytic reduction of CO₂

The photocatalytic CO₂ reduction was carried out in a SGY-I photochemical reactor (Nanjing Stonetech Electric Equipment Co., Ltd.). A 300 W Xe lamp was used as the light source and the UV light was removed by a UV cut-off filter. 200 mL NaOH (0.25 mol/L) and Na₂SO₃ (0.1 mol/L) aqueous solution was used to maintain an alkaline environment in the reaction process, and 2.0 g/L Cu/BiYO₃ catalysts were added into the reactor. Before illuminating, CO₂ flowed into the reactor at 100 mL/min for 0.5 h with solution stirring to reach an absorption equilibrium. During the reaction process, about 5.0 mL of the reaction suspension was extracted every 1.0 h [29]. The products, HCHO, CO and HCOOH were produced in this reaction process, however, the HCOOH was the main product which yield was much higher than that of HCHO and CO. Therefore, HCOOH was detected to evaluate the photocatalytic activity of catalysts by a TU-1901 dual beam UV-vis spectrophotometer (Beijing Purkinje General Instrument Co., Ltd) according to the method described in the literature [30].

2.3. Characterization

XRD was conducted on a Bruker D8 Advance X-ray diffractometer with a Cu K α radiation at 36 kV, 55 mA using a graphite monochromator. The oxidation state and surface composition were analyzed using an X-ray photoelectron spectrometer (XPS) (Kratos Ultra Axis DLD), equipped with an Al K α radiation source, and the XPS analysis was conducted at 150 W with a pass energy of 40 eV. The FT-Raman spectroscopy was performed on a Nicolet NXR 9650 FT-Raman spectrometer with the excitation wavelength at 1064 nm. The morphology of photocatalysts was investigated

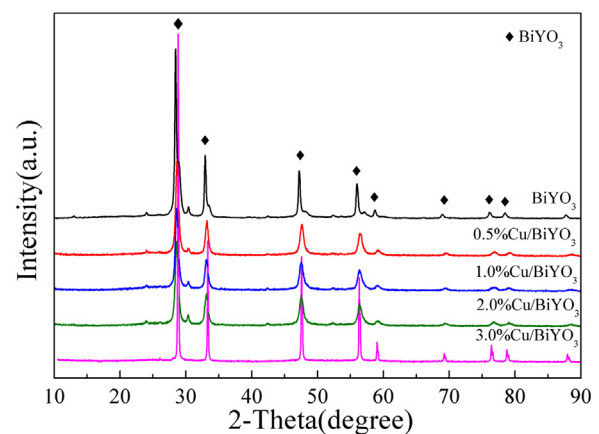


Fig. 1. XRD patterns of BiYO₃ doped with different Cu amounts.

using a Hitachi SU-8020 scanning electron microscope (SEM). The particle morphology is observed with a Tecnai G2F30 (JEOL, Japan) transmission electron microscopy (TEM) at an accelerating voltage of 300 kV. N₂ adsorption/desorption was conducted using a Micromeritics TriStar II 3020 surface area and porosity analyzer with N₂ (at 77.3 K) as sorbate. The surface areas were calculated by the Brunauer-Emmett-Teller (BET) method and the pore size distributions were evaluated by using the standard Barrett-Joyner-Halenda (BJH) method. The UV-vis diffuse reflection spectrum was conducted by a TU-1901 dual beam UV-vis spectrophotometer (Beijing Purkinje General Instrument Co., Ltd.) with BaSO₄ used as the reflectance standard. Photoluminescence (PL) spectra were measured on a RF-5301PC fluorescence spectrophotometer, and the excitation wavelength was 316 nm. Electrochemical impedance spectroscopy was performed with a CHI 660C electrochemical station in a standard three electrodes configuration, samples as the working electrodes, platinum plate as the counter electrode, and Ag/AgCl electrode as the reference electrode.

3. Results and discussion

3.1. XRD analysis

XRD patterns of BiYO₃ doped with different Cu amounts prepared via a hydrothermal method were shown in Fig. 1. The diffraction peaks at $2\theta = 28.58^\circ$, 33.01° , 47.36° , 56.14° , 58.85° , 69.06° , 76.44° , and 78.69° are corresponding to the planes (111), (200), (220), (311), (222), (400), (331), and (420) of BiYO₃ (JCPDF Card No.27-1047) [31], respectively, indicating that BiYO₃ can be obtained by a hydrothermal method with or without adding the Cu. No clear diffraction peak of CuO was observed in these XRD patterns, which most likely imply that the incorporation of CuO was low or was in an amorphous form in the catalysts [2]. On the basis of the data of the line broadening at half the maximum intensity (full width at half-maximum, FWHM) and the Bragg angle (θ), the Sherrer equation was used to calculate the mean crystallite sizes of the BiYO₃. The crystallite sizes of BiYO₃(111) for BiYO₃ with a Cu amount of 0, 0.5, 1.0, 2.0, and 3.0% Cu/BiYO₃ photocatalysts were 18.02, 17.59, 17.07, 17.03, and 44.51 nm, respectively. In addition, the diffraction peaks at 47.36° , 56.14° in 0.5, 1.0, and 2.0% Cu/BiYO₃ were broaden, and red shift of diffraction peaks were observed compared to that of BiYO₃. Based on the cubic structure of Cu/BiYO₃ and the XRD data in Fig. 1, the lattice constants of the Cu/BiYO₃ was calculated. The lattice constants (a) of the 0, 0.5, 1.0, 2.0, and 3.0% Cu/BiYO₃ photocatalysts was 5.4443 Å, 5.3967 Å, 5.4127 Å, 5.4077 Å, and 5.4577 Å, respectively. When the Cu doping amount was 0.5, 1.0, and 2.0%, the lattice constants a

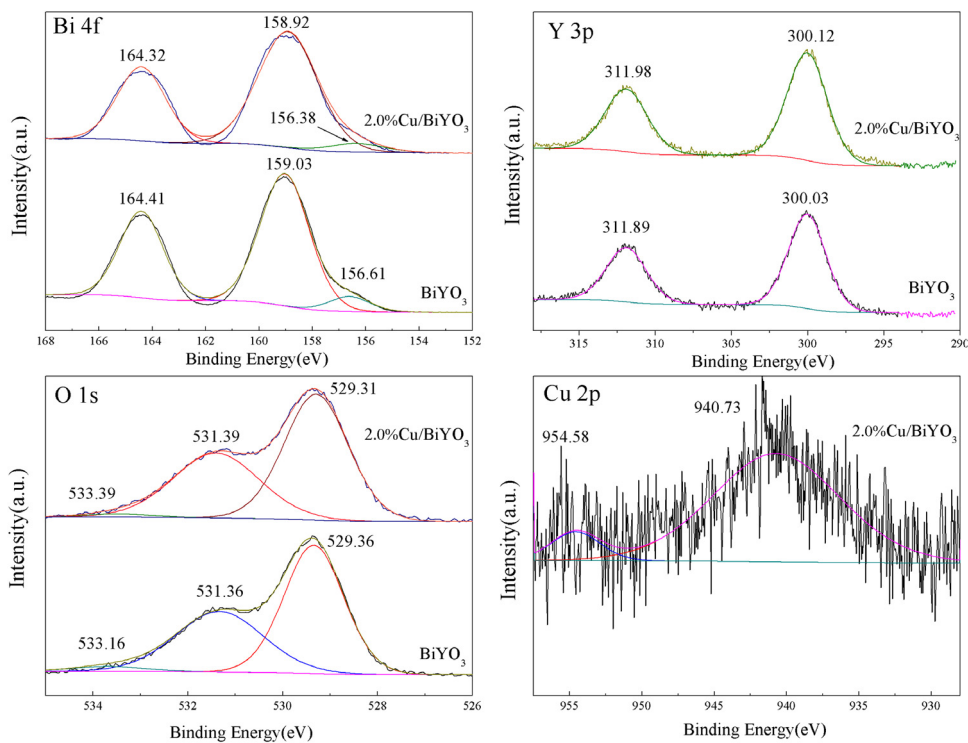


Fig. 2. The XPS spectra of Bi 4f, Y 3p, O 1s and Cu 2p of BiYO₃ and 2.0% Cu/BiYO₃.

Table 1
BE (eV) of Core Electrons of BiYO₃ and 2.0% Cu/BiYO₃.

XPS spectra	Element valence	BE (percent of valence state, %)	
		BiYO ₃	2.0% Cu/BiYO ₃
Bi 4f	Bi ³⁺ (Bi 4f _{7/2})	164.41(34.63)	164.32(34.75)
	Bi ³⁺ (Bi 4f _{5/2})	159.03(59.67)	158.92(62.07)
	Bi ³⁺ (Bi 4f _{7/2})	156.61(5.71)	156.38(3.19)
Y 3p	Y ³⁺ (Y 3p _{3/2})	311.89(38.28)	311.98(35.60)
	Y ³⁺ (Y 3p _{1/2})	300.03(61.72)	300.12(64.40)
Cu 2p	Cu ²⁺ (Cu 2p _{1/2})	–	954.58(9.41)
	Cu 3d	–	940.73(90.59)
O 1s	OH [–]	531.36(39.68)	531.39(37.59)
	O [–]	533.16(2.70)	533.39(2.52)
	O ^{2–}	529.36(57.62)	529.31(59.89)

of the Cu/BiYO₃ was smaller than that of BiYO₃. These results can be attributed to that the radius of Cu²⁺ (0.073 nm) was smaller than that with respect to Bi³⁺ (0.096 nm), the Cu/BiYO₃ cell suffers a progressive contraction when the Bi³⁺ in the BiYO₃ lattice was substituted by Cu²⁺ [32], which caused the red shift of diffraction peak according to Bragg equation [33]. When the Cu doping amount increased to 3.0%, much more Cu²⁺ entered into the lattice of the BiYO₃, resulting in the lattice expansion and the lattice constants increased to 5.4577 Å.

3.2. XPS analysis

The XPS analysis was carried out to identify the surface elements chemical states of BiYO₃ and 2.0% Cu/BiYO₃, the results were shown in Fig. 2 and listed in Table 1. As shown in Fig. 2, the two peaks for BiYO₃ (164.4 eV, 159.0 eV) and 2.0% Cu/BiYO₃ (164.3 eV, 158.9 eV), which both corresponded to Bi 4f_{7/2} [34], and the peak centered at about 156.4 eV (2.0% Cu/BiYO₃) and 156.6 eV (BiYO₃) correspond to Bi 4f_{5/2} [35], indicating that Bi existed as the form of Bi³⁺ in BiYO₃ and 2.0% Cu/BiYO₃. Blue shift of Bi 4f_{7/2} and Bi 4f_{5/2} was observed in the spectra of 2.0% Cu/BiYO₃ in comparison with the BiYO₃, which may cause by the electron transfer from Cu to Bi [36]. For the Y

3p spectra, the peaks centered at about 312.0 eV and 300.0 eV are attributed to Y 3p_{3/2} and Y 3p_{1/2} of Y³⁺ species [37], respectively. In the Cu 2p spectrum, the peak at 954.6 eV corresponded to the Cu 2p_{1/2}, indicating the existence of CuO with the +2 oxidation state of Cu in 2.0% Cu/BiYO₃ [38], and the peak at 940.73 eV was the satellite peaks in the Cu 2p region [39].

In the O 1s spectrum, the binding energies at 529.3 eV, 531.4 eV, and 533.2 eV was attributed to the oxygen in the lattice (O^{2–}) [40,41], the oxygen in the hydroxyl group on the photocatalyst surface [42], and the oxygen absorbed on the surface (O[–]) [41,42], respectively. These oxygen species played an important role in the photocatalytic reaction [43–45]. The photo electron could be captured by the adsorbed oxygen species, which will prevent the photocatalytic reduction reaction [46]. In addition, the chemisorbed oxygen on the surface, such as the surface hydroxyl groups are the scavengers of photo-induced holes, which would generate the hydroxyl free radicals (·OH) via a photocatalytic process. And an oxidation reaction can easily initiate by the ·OH, which is a strong oxidant. The physical adsorbed oxygen species, such as O₂, acts as a scavenger of photo-induced electrons. Therefore, more photo-induced electron would be captured with the increasing the amount of the physical adsorbed oxygen, which will inhibit the photocatalytic reduction reaction [46]. The amount of the total adsorbed oxygen species (including the surface hydroxyl oxygen and surface adsorbed oxygen) of 2.0% Cu/BiYO₃ was 41.10%, which was lower than that of the BiYO₃ (42.38%), therefore, the photocatalytic activity for CO₂ reduction by 2.0% Cu/BiYO₃ would be better than BiYO₃.

3.3. FT-Raman spectra analysis

The FT-Raman spectra of BiYO₃ doped with different Cu amounts were shown in Fig. 3. From Fig. 3, two typical vibrational peaks centered at 635 cm^{–1} and 103 cm^{–1} were observed for all the samples, which were attributed to B_g mode of CuO [47,48] and the external vibrating of Bi–O for BiYO₃ [31], respectively. A new peak appears at

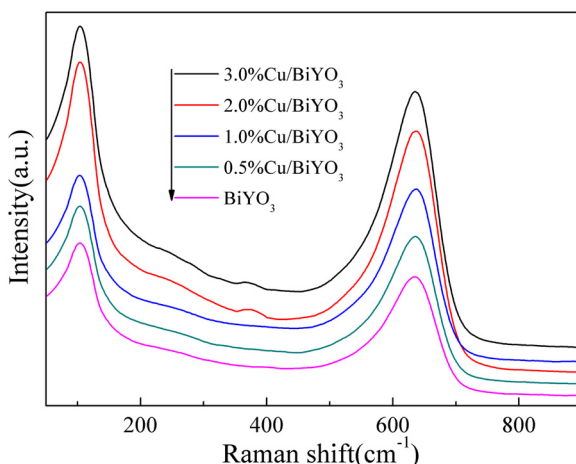


Fig. 3. FT-Raman spectra of BiYO_3 doped with different Cu amounts.

376 cm^{-1} in the spectra of 2.0% Cu/ BiYO_3 and 3.0% Cu/ BiYO_3 , and the intensity of the peak increased with the increasing of the Cu amount, which attributed to the formation of oxygen vacancies due to the presence of Cu^{2+} and Bi^{3+} in the BiYO_3 lattice [49], which could greatly facilitate the separation of photo-generated carriers of BiYO_3 .

3.4. SEM analysis

Surface and internal morphologies of the BiYO_3 doped with different Cu amounts were observed through SEM (Fig. 4). Fig. 4A shows that the BiYO_3 photocatalyst was irregularly-shaped sheet morphology, and the doped BiYO_3 shows granular-shape with more uniform size. Numerous pores can be seen in the Cu/ BiYO_3 which should be beneficial to increase the contact area for reactant diffusivity and for enhanced photocatalytic activity. Compared with BiYO_3 , the Cu/ BiYO_3 becomes less sheet and more granular in nature. Cu dosage affected the morphology of the composites. When the Cu doped amount reached 2.0%, the 2.0% Cu/ BiYO_3 presents a more homogeneous surface, more uniform particles and better dispersity, and the particle size was the smallest in comparison with the other Cu/ BiYO_3 . However, excessive amounts of Cu dopant resulted in agglomeration of BiYO_3 . Based on the porous structure of 2.0% Cu/ BiYO_3 , the 2.0% Cu/ BiYO_3 could provide more sites and an efficient pathway for reactants accessing the photocatalytic active center, which was expected to greatly strengthen the photocatalytic conversion of CO_2 on the Cu/ BiYO_3 . Combine with the analysis of surface area for Cu/ BiYO_3 , the surface area increased markedly with a decrease in particle size. For example, the surface area of the 2.0% Cu/ BiYO_3 ($18.64 \text{ m}^2/\text{g}$) was 2.8 times higher than that of the BiYO_3 ($6.75 \text{ m}^2/\text{g}$), indicating the Cu-doping in BiYO_3 would benefit the decreasing of the particle size and increasing of the surface area.

3.5. Microstructural studies by TEM

The morphology and microstructural details of the BiYO_3 and 2.0% Cu/ BiYO_3 were investigated by TEM, HRTEM, EDS, and SAED observation. Fig. 5A show that BiYO_3 was irregularly-shaped sheet with a size from 15 nm to 140 nm, coinciding with the results from SEM images. Fig. 5B represents the corresponding HRTEM image and the SAED patterns (inset (b) in Fig. 5B). A magnified region of the HRTEM image was shown in the inset (a) in Fig. 5B and illustrated the interplanar spacing of 0.31 nm, which conformed to the (111) crystal planes of BiYO_3 . The BiYO_3 was

found to be in a well-crystallized form as shown by the selected area electron diffraction (SAED) analysis. Furthermore, SAED image show distinct electron diffraction rings, confirming the assembly of polycrystallites of the sample. For 2.0% Cu/ BiYO_3 , many granular-shape Cu/ BiYO_3 nanoparticles with sizes from 15 to 40 nm were observed (Fig. 5C), which is consistent with the SEM observation. From the HRTEM of the 2.0% Cu/ BiYO_3 , the discerned interplanar spacing of 0.31 and 0.28 nm conformed to the (111) and (200) crystal planes of BiYO_3 (Fig. 5E), which indicated the particles were having orientations along (111) and (200) planes. The SAED pattern (inset in Fig. 5D) indicated a polycrystalline area consisting of several small, randomly oriented crystallites, generating bright spots which form concentric diffraction rings, specific to different crystalline planes. In addition, the composition of these samples were determined by the EDS (Fig. 5F). The EDS image verified that the sample composed of the elements of Cu, Bi, Y, and O.

3.6. Specific surface areas and pore structure analysis

The N_2 adsorption-desorption isotherm and the pore size distribution curves of BiYO_3 and BiYO_3 doped with different Cu amounts are shown in Fig. 6, and the specific surface areas and pore size of the samples are listed in Table 2. It can be found that the N_2 adsorption isotherm of BiYO_3 , 0.5% Cu/ BiYO_3 , 1.0% Cu/ BiYO_3 , and 2.0% Cu/ BiYO_3 were classified as a IV-type isotherm. At the low pressure section ($P/P_0 = 0\text{--}0.8$), the adsorption capacity of N_2 increased slowly with the increase of relative pressure, which indicated that the adsorption of N_2 molecules on the surface of the photocatalyst was converted to a multi-layer adsorption [50]. At the high pressure section ($P/P_0 = 0.8\text{--}1.0$), the isotherms obtained by desorption were not coincident with the adsorption isotherms, which distributed to the occurrence of capillary condensation. However, hardly any nitrogen adsorbs on the 3.0% Cu/ BiYO_3 .

In general, the larger specific surface area of the sample can provide more absorption and/or active sites for reactant, which results in higher photocatalytic activity [51]. From Table 2, the specific surface area of BiYO_3 with a Cu amount of 0, 0.5, 1.0, and 2.0% Cu/ BiYO_3 was 6.75, 15.51, 18.04, and $18.64 \text{ m}^2/\text{g}$, and the corresponding pore size was 4.72 nm, 21.03 nm, 21.10 nm, 16.26 nm, respectively, the pore size was in the range of 2–50 nm, indicating these samples are mesoporous structure. Among these catalysts, 2.0% Cu/ BiYO_3 exhibited the largest specific surface area than the other samples, combined with the results of the SEM, when the Cu amount was 2.0%, the particle size of BiYO_3 was the smallest. However, the specific surface area of 3.0% Cu/ BiYO_3 was only $0.61 \text{ m}^2/\text{g}$, which was smallest compared with the other samples, which were consistent with the N_2 adsorption-desorption isotherm. When the Cu amount exceeded 2.0%, the excess Cu would enter and block the pore of BiYO_3 catalysts, causing the sharply decrease of the pore size and the specific surface area [52]. Obviously, doping Cu affected the surface areas and the pore size distributions of BiYO_3 catalyst, and the BiYO_3 specific surface area increased firstly, and subsequently decreased with the increasing of Cu amount.

3.7. UV-vis diffuse reflectance spectra analysis

The UV-vis diffuse reflectance spectra of BiYO_3 , BiYO_3 doped with different Cu amounts were shown in Fig. 7. From Fig. 7, the Cu/ BiYO_3 samples show a significant enhancement of optical absorption between 400 and 700 nm than that of BiYO_3 . The absorbed edge of the BiYO_3 and 0.5% Cu/ BiYO_3 , 1.0% Cu/ BiYO_3 , 2.0% Cu/ BiYO_3 , and 3.0% Cu/ BiYO_3 was 517, 534, 540, 549, and 529 nm, respectively, indicating a red shift of the absorbed edges after doping with Cu. Furthermore, the optical absorbance of the Cu/ BiYO_3

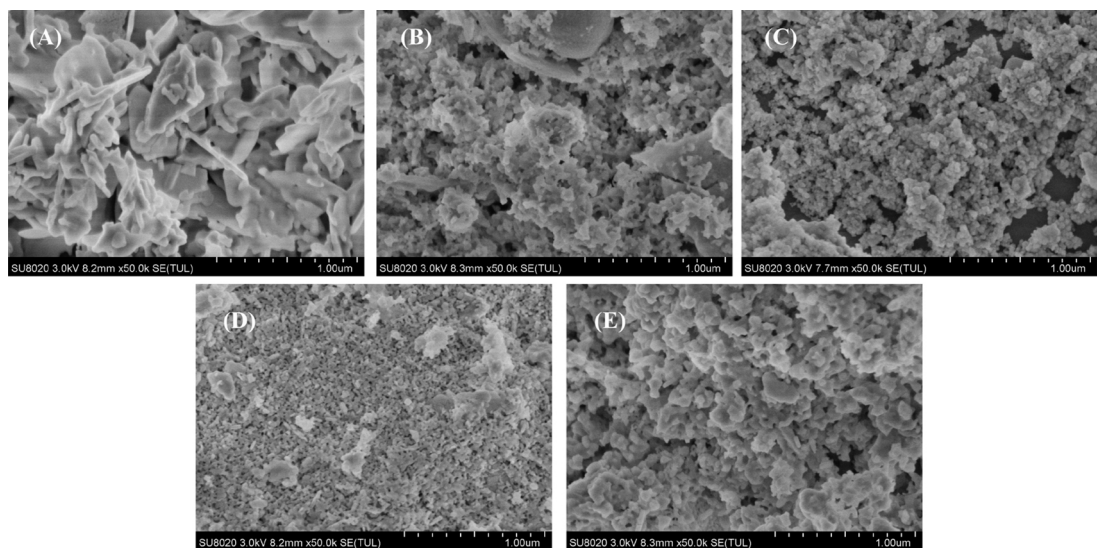


Fig. 4. SEM images of Cu/BiYO₃ with a Cu amount of 0(A), 0.5 (B), 1.0 (C), 2.0 (D), and 3.0%(E).

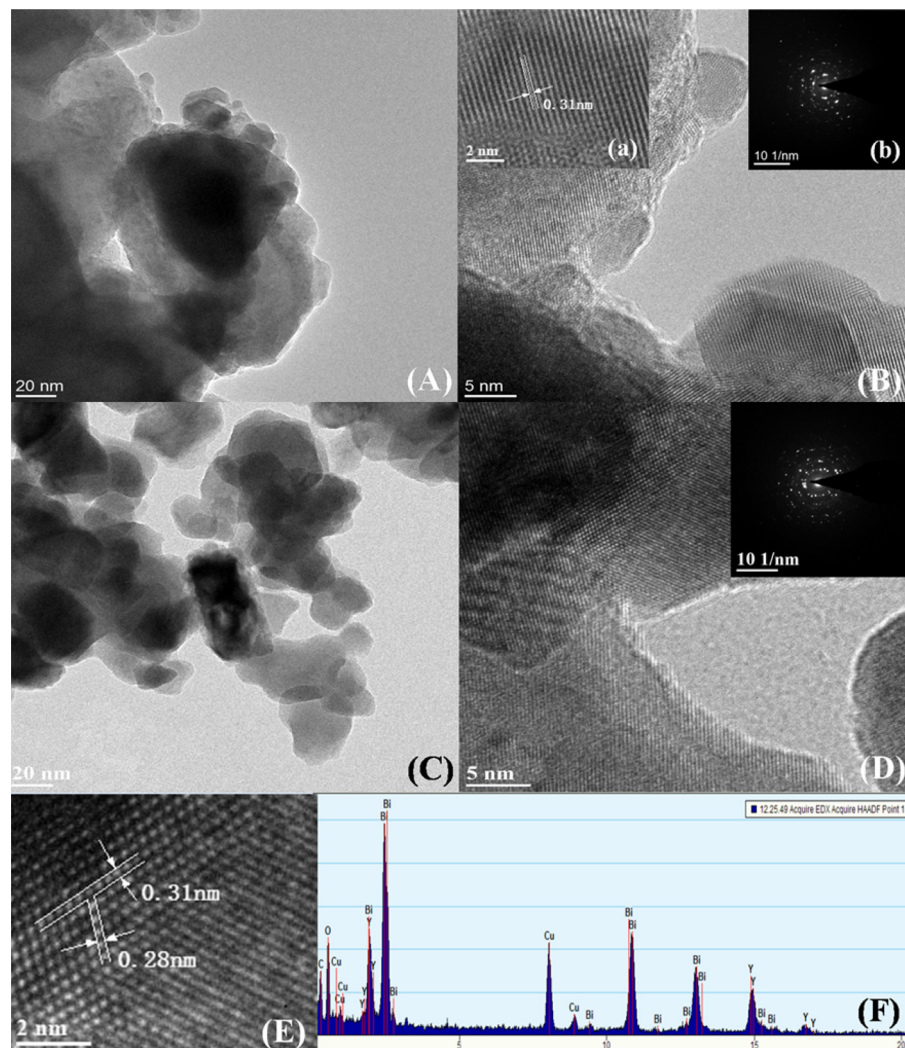


Fig. 5. TEM image(A), HRTEM image (B) of BiYO₃ and TEM image (C), HRTEM image (D, E), EDS (F) of 2.0% Cu/BiYO₃, and the inset in (B) and (D) are SAED patterns.

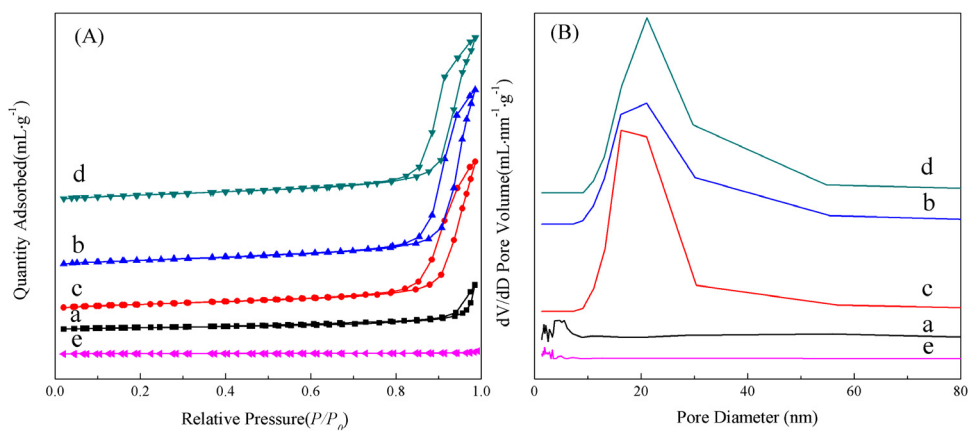


Fig. 6. Nitrogen adsorption/desorption isotherms (A) and pore size distribution curves (B) of Cu/BiYO₃ with a Cu amount of 0 (a), 0.5 (b), 1.0 (c), 2.0 (d), and 3.0% (e).

Table 2

Textural properties of BiYO₃ and BiYO₃ doped with different Cu amounts.

Amount of Cu (%)	BET surface area (m ² /g)	Pore diameter (nm)	Pore volume (mL/g)
0	6.75	4.72	0.034
0.5	15.51	21.03	0.112
1.0	18.04	21.10	0.135
2.0	18.64	16.26	0.126
3.0	0.61	1.92	0.003

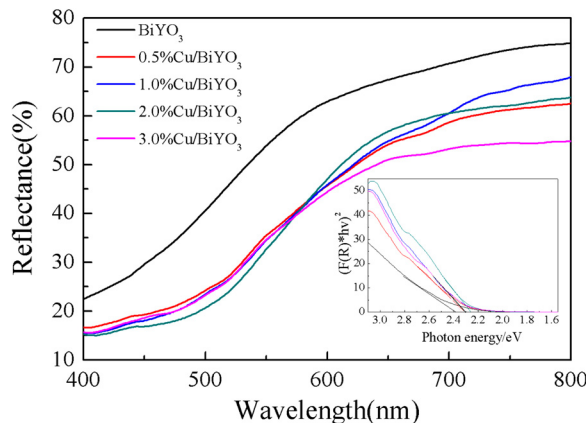


Fig. 7. UV-vis diffuse reflectance spectra of BiYO₃ doped with different Cu amounts, the inset is the absorbance of samples from reflectance by Kubelka–Munk method.

was predicted by the Kubelka–Munk function [53,54], as shown in the inset of Fig. 7. Based on the Kubelka–Munk method, the band gap of the BiYO₃ and 0.5% Cu/BiYO₃, 1.0% Cu/BiYO₃, 2.0% Cu/BiYO₃, and 3.0% Cu/BiYO₃ was 2.39, 2.32, 2.30, 2.26, and 2.34 eV, respectively. In the preparation process, Cu²⁺ could replace Bi³⁺ and enter the BiYO₃ lattice, and 3d electron orbit of Cu was not full of extra nuclear electrons [55,56], orbital electrons were more likely to transmit to the BiYO₃ conduction band when excited by the visible light, which was in accordance with the XPS analysis. And the replace of Cu²⁺ to Bi³⁺ may form the oxygen vacancies in the structure of BiYO₃ [33]. Furthermore, the electron density of Bi increased due to the lower electronegativity of the doping Cu. Therefore, the valence electron transfers to the Bi atom and the hybrid orbital of Bi 6s and O 2p became narrow down [57,58], which increased the activity of photo electrons and holes and it is easier for electronic transition after being photo-excited, so it is beneficial to the enhancement of the photocatalytic activity of BiYO₃ [59].

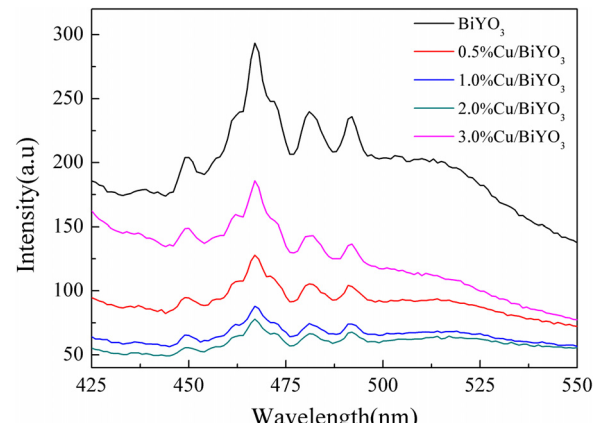


Fig. 8. Photoluminescence spectra of BiYO₃ doped with different Cu amounts.

3.8. Photoluminescence spectra analysis

Photoluminescence (PL) spectra are usually used to analyze the separation efficiency of charge carriers, and it is very helpful to understand the fate of electron–hole pairs in semiconductor as PL emission arises from the recombination of free carriers, and a low PL intensity is generally indicative of a high separation efficiency of electron–hole pairs [60]. The PL spectra of the BiYO₃ and Cu/BiYO₃ with 316 nm excitation wavelength were displayed in Fig. 8, broad emission peak was observed in BiYO₃ and Cu/BiYO₃ doped with different Cu amounts, which is attributed to the recombination of electron and hole [48]. The shapes and peaks positions of Cu/BiYO₃ samples are similar to the BiYO₃, while the intensity of this emission peak for Cu/BiYO₃ samples was substantially low after inducing Cu. This drastic quenching of the emission clearly indicates the introduced Cu can greatly facilitate the separation of photo-generated carriers of BiYO₃. In addition, the emission band intensities of the spectra vary for the Cu/BiYO₃ doped with

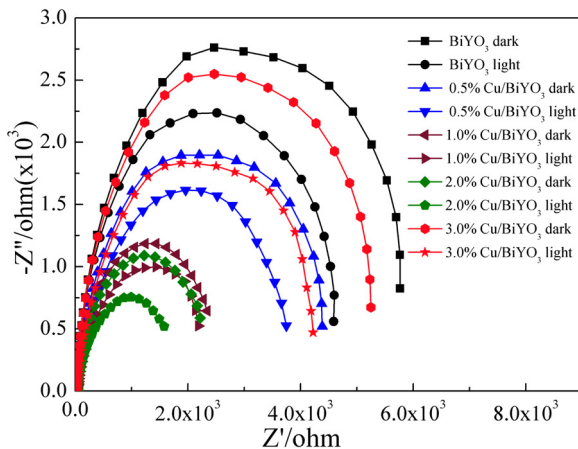


Fig. 9. Electrochemical impedance spectra of BiYO_3 doped with different Cu amounts in the darkness and under visible light irradiation.

different Cu amounts. Furthermore, the 2.0% Cu/BiYO₃ show significantly diminished PL intensity in comparison with the other Cu/BiYO₃ samples, indicating that the 2.0% Cu/BiYO₃ have the lowest electron-holes recombination and may exhibit better photocatalytic activity than undoped BiYO₃ (Fig. 8).

3.9. Electrochemical impedance spectroscopy analysis

It is well known that electrochemical impedance spectroscopy (EIS) has proven to be beneficial for characterizing charge transport properties, and the reaction rate occurring at the surface of the electrodes can be analyzed by the arc radius on the Nyquist plot [60,61]. The smaller the arc radius of the EIS Nyquist plot, the lower the electric charge transfer resistance. Fig. 9 shows the EIS Nyquist plots of BiYO₃ and Cu/BiYO₃ samples in the darkness and under visible light irradiation. From Nyquist plots (Fig. 9), the arc radius of all samples after visible light irradiation was smaller than those in the darkness, revealing that the photo-generated carriers were generated. More importantly, the arc radius of Cu/BiYO₃ samples was obviously smaller than that of BiYO₃, indicating that the resistance of charge transport on the surface of the BiYO₃ was reduced by doping with Cu. Cu²⁺ could replace Bi³⁺ and enter into the BiYO₃ lattice, which greatly improves the charge transfer and inhibits the recombination of the photo-generated electrons and holes, thus promoting the separation efficiency of the photo-generated carriers. Furthermore, the arc radius of 2.0% Cu/BiYO₃ after visible light irradiation was the smallest compared with the other catalyst, suggesting the effective separation of photo-generated carriers over 2.0% Cu/BiYO₃.

3.10. Photocatalytic reduction of CO_2

The photosynthesis performance of BiYO₃ and BiYO₃ doped with different Cu amounts were shown in Fig. 10. Fig. 10A shows that the photocatalytic reduced HCOOH amount by using BiYO₃, 0.5% Cu/BiYO₃, 1.0% Cu/BiYO₃, 2.0% Cu/BiYO₃, and 3.0% Cu/BiYO₃ was 0.92, 1.43, 1.62, 2.04, and 1.17 $\mu\text{mol}/\text{mL}$, respectively, and no HCOOH was detected in the dark condition or without the catalyst. Obviously, there was an enhancement of photocatalytic activity after doping with Cu. The photocatalytic activity of the 2.0% Cu/BiYO₃ was the highest, and the amount of HCOOH from photocatalytic reduction of CO_2 using 2.0% Cu/BiYO₃ was 2.2 times than that of the undoped BiYO₃. Combined with the results of characterization, the oxygen vacancies was formed in the structure of BiYO₃ when the Cu²⁺ replaced the Bi³⁺ in the BiYO₃ lattice [33]. These oxygen vacancies may act as electron capture centers, which play

an important role in retarding the recombination of photo-induced electron and hole, and can improve the photocatalytic activity of BiYO₃ [62–64]. Furthermore, the electron transfers from Cu atom to the Bi atom and resulted in the binding energy of the inner layer electron decreased [36], then the band gap of the BiYO₃ photocatalysts decreased. When the amount of Cu was lower than the 2.0%, the BiYO₃ particle size decreased, and the specific surface area and the photocatalytic activity increased gradually with the increase of Cu amount. Nevertheless, when the amount of Cu exceeded the 2.0%, the excess Cu would cover the surface of the BiYO₃ and block the pore of BiYO₃, which led to the photocatalytic activity was decreased [65]. Among all the BiYO₃ photocatalysts, 2.0% Cu/BiYO₃ had a higher specific surface area ($18.64 \text{ m}^2/\text{g}$) and larger visible light absorbed edge (549 nm) or lower band gap (2.26 eV), which greatly increases the adsorption capacity of CO_2 , and provides more active site on the photocatalyst surface. In addition, the transfer rate of the photo-generated electron and hole was accelerated, therefore, the recombination of photo-generated electron and hole was depressed, which led to a higher photocatalytic reduction activity [59]. Fig. 10B shows the stability of the 2.0% Cu/BiYO₃ catalyst on the CO_2 photocatalytic reduction. In the same conditions, the HCOOH yield was 2.04 $\mu\text{mol}/\text{mL}$ after the 1st round reaction, and even after 5 successive cycles, the HCOOH yield was only reduced 8.3%–1.87 $\mu\text{mol}/\text{mL}$, which indicated the 2.0% Cu/BiYO₃ catalyst maintains a good stability after a 5-time reaction. Therefore, the 2.0% Cu/BiYO₃ exhibits excellent performance stability, with strong resistance to morphology and composition changes.

3.11. Characterization of 5-time used 2.0% Cu/BiYO₃

To investigate the change of the 2.0% Cu/BiYO₃ catalyst after 5 times used, XRD, UV-vis diffuse reflectance spectra, Nitrogen adsorption/desorption were conducted, and the results were shown in Fig. 11. After used for five times, no significant change was found on the XRD pattern of the 2.0% Cu/BiYO₃ compared to that before reaction in Fig. 1, however, the crystallite size of (111) plane of BiYO₃ in the 2.0% Cu/BiYO₃ was increased from 17.03 nm to 51.61 nm, which indicated that the crystallite size of BiYO₃ was increased during the reaction process. From Fig. 11C, the N_2 adsorption isotherm of 2.0% Cu/BiYO₃ used five times was almost the same to the fresh one (shown in Fig. 6), and the pore distribution become narrow, and the BET surface area, pore diameter, and pore volume of the 2.0% Cu/BiYO₃ after 5 times reused was $16.25 \text{ m}^2/\text{g}$, 18.72 nm, and 0.118 mL/g , respectively, which was slight decrease compared to the fresh 2.0% Cu/BiYO₃. In addition, the band gap slightly changed from 2.26 eV to 2.31 eV, which would reduce the light absorption on the catalysts. These results would decrease the photocatalytic activity of 2.0% Cu/BiYO₃, which is consistent with the experimental results. The XPS spectra of 2.0% Cu/BiYO₃ used five times was shown in Fig. 12, and the binding energies of the Bi 4f, Y 3p, Cu 2p, and O1s was change in the range of 0.03–0.42 eV (Table 3), however, the oxidation state of the Bi, Y, Cu, and O was remained unchanged, which indicated that the state of active sites was the same to that of the 2.0% Cu/BiYO₃ before reaction.

3.12. Reaction mechanism

Based on our obtained experimental results and reports in the literature [29,66,67], the possible reaction mechanism for photocatalytic reduction of CO_2 is shown in Fig. 13. Under the irradiation of light source, photogenerated holes were produced in the valence band (VB) of Cu/BiYO₃, which should be more positive than the oxidation potential of $\text{O}_2/\text{H}_2\text{O}$, oxidize water to O_2 and release H^+ , and photogenerated electrons were produced in the conduction band (CB) of Cu/BiYO₃ to reduce CO_2 to $\cdot\text{CO}_2^-$, then the $\cdot\text{CO}_2^-$ reacted with the H^+ to produce HCOOH by a sequence of reactions. In gen-

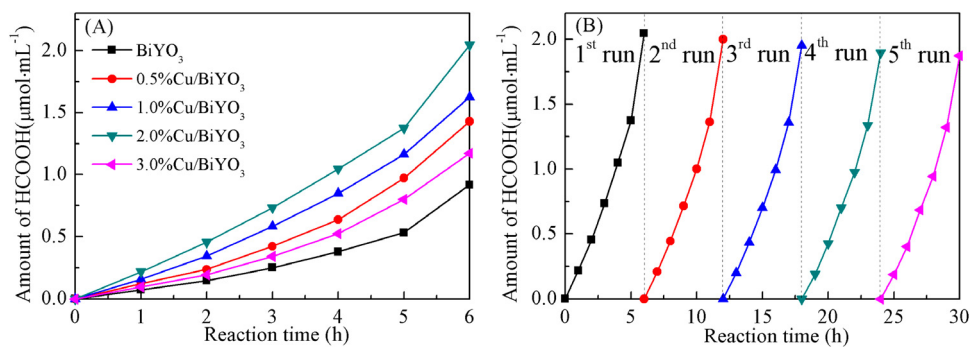


Fig. 10. (A) Photosynthesis performance of BiYO₃ doped with different Cu amounts. (B) Cycling performance of photocatalytic reduction of CO₂ over 2.0% Cu/BiYO₃.

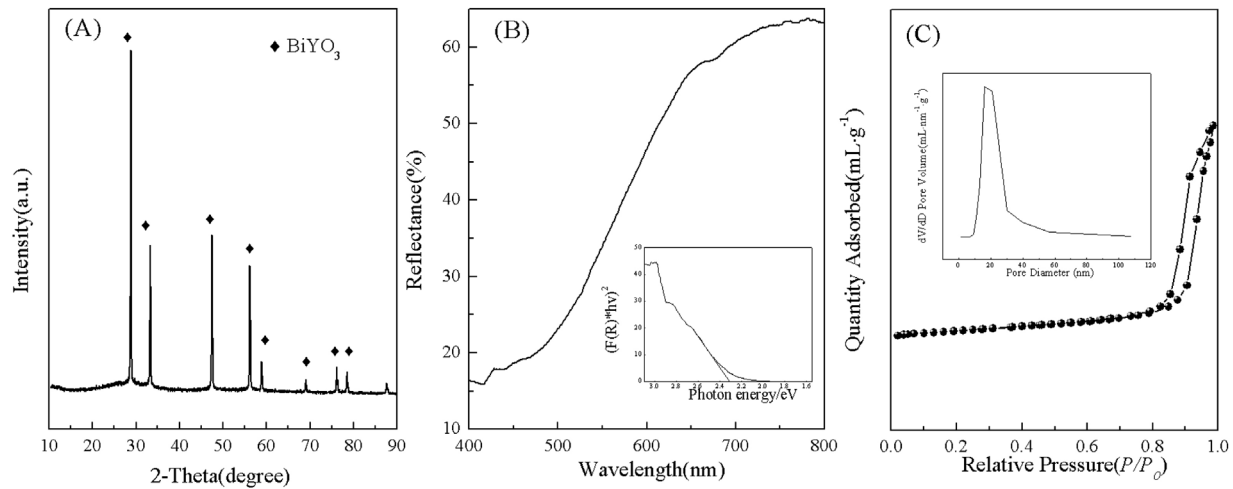


Fig. 11. The XRD patterns (A), UV-vis diffuse reflectance spectrum (B), Nitrogen adsorption/desorption isotherms and pore size distribution curves (inset) (C) of 2.0% Cu/BiYO₃ repeated use for five times.

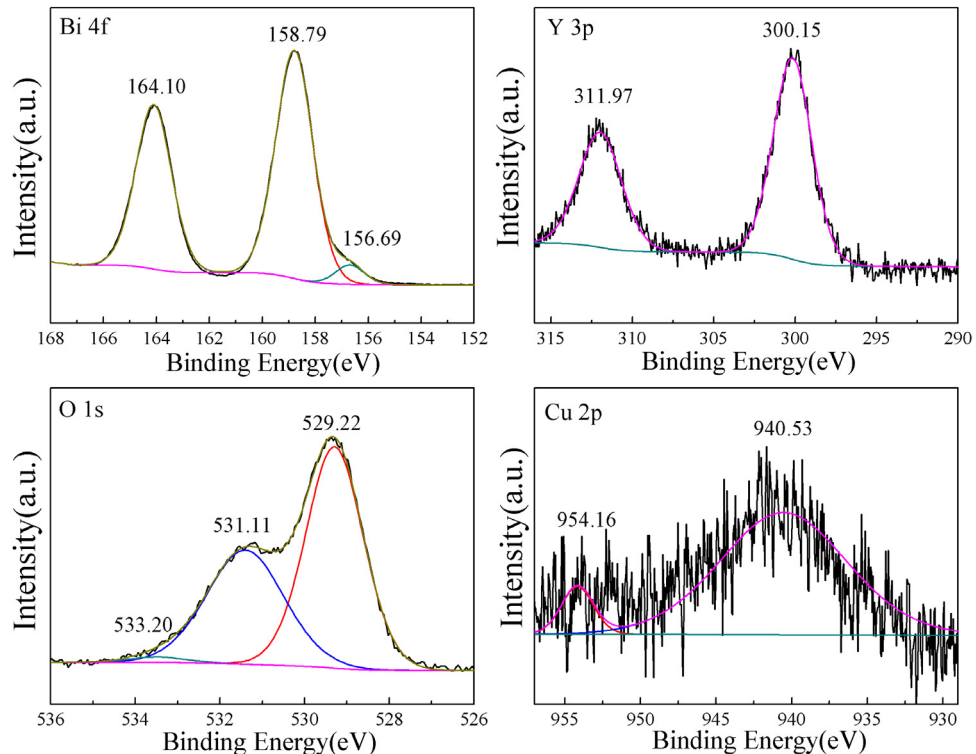
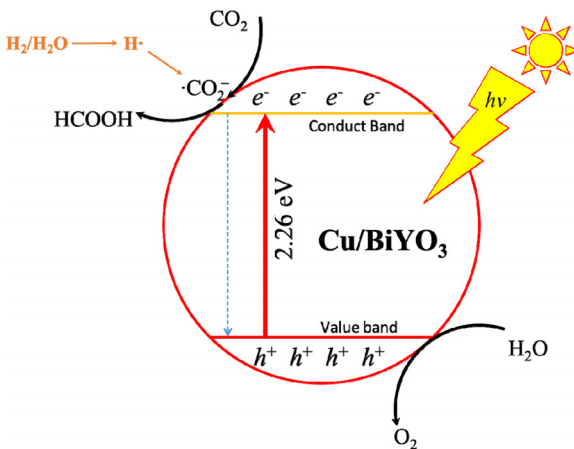


Fig. 12. The XPS spectra of Bi 4f, Y 3p, O 1s and Cu 2p of 2.0% Cu/BiYO₃ repeated use for five times.

Table 3BE (eV) of core electrons of 2.0% Cu/BiYO₃ after 5-time used.

XPS spectra	Element valence	BE (percent of valence state, %)
Bi 4f	Bi ³⁺ (Bi 4f _{7/2})	164.10(56.82)
	Bi ³⁺ (Bi 4f _{5/2})	158.79(39.42)
	Bi ³⁺ (Bi 4f _{7/2})	156.69(3.76)
Y 3p	Y ³⁺ (Y 3p _{3/2})	311.97(38.78)
	Y ³⁺ (Y 3p _{1/2})	300.15(61.22)
Cu 2p	Cu ²⁺ (Cu 2p _{1/2})	954.16(9.03)
	Cu 3d	940.53(90.97)
O 1s	OH [−]	531.11(41.37)
	O [−]	533.20(6.53)
	O ^{2−}	529.22(50.90)

**Fig. 13.** Possible mechanism of photoreduction CO₂ to HCOOH on Cu/BiYO₃.

eral, the CO₂ is absorbed on the Cu/BiYO₃ surface and became a distorted molecule and then reduced to HCOOH in the surface of the Cu/BiYO₃.

4. Conclusions

In summary, BiYO₃ and BiYO₃ doped with different Cu amounts were successfully synthesized via hydrothermal method. These Cu/BiYO₃ exhibit enhanced photocatalytic activities for the photocatalytic reduction of CO₂ under the visible light irradiation. And the 2.0% Cu/BiYO₃ shows the best photocatalytic activity, and the photocatalytic reduced HCOOH amount (2.04 μmol/mL) was 2.2 times than that (0.92 μmol/mL) of the undoped BiYO₃. Doping with Cu would be beneficial for the decrease of particle size and increase of the surface area, the light absorption was increased, and the resistance of charge transport on the surface of the BiYO₃ was reduced by doping with Cu. Cu²⁺ could replace Bi³⁺ and enter the BiYO₃ lattice and the oxygen vacancies were generated. The highly improved performance of the 2.0% Cu/BiYO₃ can be ascribed to the reduced band-gap energies, oxygen vacancies, and the efficient charge separation.

Acknowledgments

This work was supported by the National Natural Science Foundation of China (21366004, 21425627), Guangxi Natural Science Foundation (2015GXNSFDA139005), the Open Project of Guangxi Key Laboratory of Petrochemical Resource Processing and Process Intensification Technology (2015K004).

References

- [1] M. Li, L. Zhang, M. Wu, Y. Du, X. Fan, M. Wang, L. Zhang, Q. Kong, J. Shi, *Nano Energy* 19 (2016) 145–155.
- [2] R.W. Liu, Z.Z. Qin, H.B. Ji, T.M. Su, *Ind. Eng. Chem. Res.* 52 (2013) 16648–16655.
- [3] P. Dhak, S.K.S. Patel, M.-K. Kim, J.-H. Lee, M. Kim, S.-K. Kim, *J. Magn. Magn. Mater.* 408 (2016) 67–72.
- [4] T. Baran, S. Wojtyla, A. Dibenedetto, M. Aresta, W. Macyk, *Appl. Catal. B* 178 (2015) 170–176.
- [5] J.-W. Wang, Y.-H. Jing, T. Ouyang, Q. Zhang, C.-T. Chang, *Catal. Commun.* 59 (2015) 69–72.
- [6] K. Tian, W.-J. Liu, H. Jiang, *ACS Sustain. Chem. Eng.* 3 (2015) 269–276.
- [7] Q. Liu, Y. Zhou, J. Kou, X. Chen, Z. Tian, J. Gao, S. Yan, Z. Zou, *J. Am. Chem. Soc.* 132 (2010) 14385–14387.
- [8] H. Li, Y. Lei, Y. Huang, Y. Fang, Y. Xu, L. Zhu, X. Li, *J. Nat. Gas Chem.* 20 (2011) 145–150.
- [9] Z. Zhao, J. Fan, M. Xie, Z. Wang, *J. Clean. Prod.* 17 (2009) 1025–1029.
- [10] R.A. He, S. Cao, P. Zhou, J. Yu, *Chin. J. Catal.* 35 (2014) 989–1007.
- [11] Q. Yuan, L. Chen, M. Xiong, J. He, S.-L. Luo, C.-T. Au, S.-F. Yin, *Chem. Eng. J.* 255 (2014) 394–402.
- [12] L.W. Shan, G.L. Wang, J. Suriyaprakash, D. Li, L.Z. Liu, L.M. Dong, *J. Alloys Compd.* 636 (2015) 131–137.
- [13] B.V. Kumar, M.D. Prasad, M. Vithal, *Mater. Lett.* 152 (2015) 200–202.
- [14] M. Wang, Y.S. Che, C. Niu, M.Y. Dang, D. Dong, *J. Rare Earths* 31 (2013) 878–884.
- [15] L. Ge, *J. Inorg. Mater.* 23 (2008) 449–453.
- [16] X.F. Zhang, Y.B. Zhang, X. Quan, S. Chen, *J. Hazard. Mater.* 167 (2009) 911–914.
- [17] Y. Wu, G. Zhang, W. Guan, X. Zhang, *Micro Nano Lett.* 9 (2014) 119–122.
- [18] J.C. Colmenares, M.A. Aramendia, A. Marinas, J.M. Marinas, F.J. Urbano, *Appl. Catal. A* 306 (2006) 120–127.
- [19] H.-y. Lin, C.-y. Shih, *J. Mol. Catal. A* 411 (2016) 128–137.
- [20] J. Xia, M. Ji, W. Li, J. Di, H. Xu, M. He, Q. Zhang, H. Li, *Colloids Surf. A* 489 (2016) 343–350.
- [21] J. Li, Z. Guo, Z. Zhu, *Ceram. Int.* 40 (2014) 6495–6501.
- [22] R. Cao, H. Huang, N. Tian, Y. Zhang, Y. Guo, T. Zhang, *Mater. Charact.* 101 (2015) 166–172.
- [23] X.M. Gao, F. Fu, W.H. Li, *Phys. B* 412 (2013) 26–31.
- [24] Y. Chen, K.-C. Zhou, S.-P. Huang, Z.-Y. Li, G.-C. Liu, *J. Inorg. Mater.* 27 (2012) 19–25.
- [25] X. Yang, N. Qu, H. Wang, B. Huang, J. Wei, *Mater. Lett.* 60 (2006) 2886–2888.
- [26] B. Fang, Y. Xing, A. Bonakdarpour, S. Zhang, D.P. Wilkinson, *ACS Sustain. Chem. Eng.* 3 (2015) 2381–2388.
- [27] I. Shown, H.-C. Hsu, Y.-C. Chang, C.-H. Lin, P.K. Roy, A. Ganguly, C.-H. Wang, J.-K. Chang, C.-I. Wu, L.-C. Chen, K.-H. Chen, *Nano Lett.* 14 (2014) 6097–6103.
- [28] Z.-z. Qin, Z.-I. Liu, Y.-b. Liu, K.-d. Yang, *Catal. Commun.* 10 (2009) 1604–1608.
- [29] Z. Qin, H. Tian, T. Su, H. Ji, Z. Guo, *RSC Adv.* 6 (2016) 52665–52673.
- [30] L.M. Xue, F.H. Zhang, H.J. Fan, B. Chen, X.F. Bai, *Min. Metall. Eng.* 31 (2011) 84–87.
- [31] F.M. Ascencio Aguirre, R. Herrera Becerra, *Appl. Phys. A* 119 (2015) 909–915.
- [32] R. Mohan, K. Krishnamoorthy, S.J. Kim, *Solid State Commun.* 152 (2012) 375–380.
- [33] R.D. Shannon, *Acta Crystallogr. Sect. A* 32 (1976) 751–767.
- [34] A.T. Kozakov, A.G. Kochur, A.V. Nikolsky, K.A. Googlev, V.G. Smotrakov, V.V. Eremkin, *J. Electron Spectrosc. Relat. Phenom.* 184 (2011) 508–516.
- [35] S. Pouston, N.J. Price, C. Weeks, M.D. Allen, P. Parlett, M. Steinberg, M. Bowker, *J. Catal.* 178 (1998) 658–667.
- [36] P.S. Bagus, E.S. Ilton, C.J. Nelin, *Surf. Sci. Rep.* 68 (2013) 273–304.
- [37] L.S.A. Fujimori, *J. Phys. C Solid State Phys.* 17 (1984) 341–351.
- [38] J.P. Espinosa, J. Morales, A. Barranco, A. Caballero, J.P. Holgado, A.R. Gonzalez-Elipe, *J. Phys. Chem. B* 106 (2002) 6921–6929.
- [39] L.X. Wang, W.C. Zhu, D.F. Zheng, X. Yu, J. Cui, M.J. Jia, W.X. Zhang, Z.L. Wang, *React. Kinet. Mech. Catal.* 101 (2010) 365–375.
- [40] W. Wang, S. Li, Y. Wen, M. Gong, L. Zhang, Y. Yao, Y. Chen, *Acta Phys. Chim. Sin.* 24 (2008) 1761–1766.
- [41] V. Abdelsayed, S. Moussa, H.M. Hassan, H.S. Aluri, M.M. Collinson, M.S. El-Shall, *J. Phys. Chem. Lett.* 1 (2010) 2804–2809.
- [42] L. Hu, Z. Du, X. Tai, Q. Li, Y. Zhao, *Chin. J. Catal.* 29 (2008) 571–576.
- [43] T.-m. Su, Z.-z. Qin, H.-b. Ji, Y.-x. Jiang, *Int. J. Photoenergy* 2014 (2014) 794057.
- [44] M.R. Hoffmann, S.T. Martin, W. Choi, D.W. Bahnemann, *Chem. Rev.* 95 (1995) 69–96.
- [45] M.-g. Fan, Z.-z. Qin, Z.-l. Liu, T.-m. Su, *Adv. Mater. Res.* 287–290 (2011) 1640–1645.
- [46] K. Sutthiuporn, S. Kawi, *Int. J. Hydrogen Energy* 36 (2011) 14435–14446.
- [47] G. Sahoo, M.K. Jain, *Appl. Phys. A* 118 (2015) 1059–1066.
- [48] J. Zhao, R. Liu, Z. Hua, *Superlattices Microstruct.* 81 (2015) 243–247.
- [49] Y. Huang, B. Long, M. Tang, Z. Rui, M.-S. Balogun, Y. Tong, H. Ji, *Appl. Catal. B* 181 (2016) 779–787.
- [50] J.L. Mendoza de la Cruz, I.V. Castellanos-Ramírez, A. Ortiz-Tapia, E. Buenrostro-González, C. d.I.A. Durán-Valencia, S. López-Ramírez, *Colloids Surf. A* 340 (2009) 149–154.
- [51] J.Q. Yu, A. Kudo, *Adv. Funct. Mater.* 16 (2006) 2163–2169.
- [52] M.R. Housaindokht, A. Nakhaei Pour, *Solid State Sci.* 14 (2012) 622–625.
- [53] J.H. Nobbs, *Rev. Prog. Color. Relat. Top.* 15 (1985) 66–75.
- [54] Z.C. Orel, M.K. Gunde, B. Orel, *Prog. Org. Coat.* 30 (1997) 59–66.
- [55] G. Colon, M. Maicu, M.C. Hidalgo, J.A. Navio, *Appl. Catal. B* 67 (2006) 41–51.

[56] S.X. Wu, Z. Ma, Y.N. Qin, F. He, L.S. Jia, Y.J. Zhang, *Acta Phys. Chim. Sin.* 19 (2003) 967–969.

[57] A.M. Dumitrescu, A.I. Borhan, A.R. Iordan, I. Dumitru, M.N. Palamaru, *Powder Technol.* 268 (2014) 95–101.

[58] Y. Li, J. Wan, Z. Gu, *Mater. Sci. Eng.: A* 286 (2000) 106–109.

[59] J.-H. Kim, F. Nishimura, S. Yonezawa, M. Takashima, *J. Fluorine Chem.* 144 (2012) 165–170.

[60] Y. Huang, W. Fan, B. Long, H. Li, F. Zhao, Z. Liu, Y. Tong, H. Ji, *Appl. Catal. B* 185 (2016) 68–76.

[61] X. Tang, X. Liu, L. Zhang, Y. Xing, Y. Tian, *Chem. Phys.* 441 (2014) 121–127.

[62] L. Renuka, K.S. Anantharaju, S.C. Sharma, H.P. Nagaswarupa, S.C. Prashantha, H. Nagabhushana, Y.S. Vidya, *J. Alloys Compd.* 672 (2016) 609–622.

[63] J.G. Wang, P.H. Rao, W. An, J.L. Xu, Y. Men, *Appl. Catal. B* 195 (2016) 141–148.

[64] C. Liu, R.R. Han, H.M. Ji, T. Sun, J. Zhao, N.N. Chen, J. Chen, X.F. Guo, W.H. Hou, W.P. Ding, *Phys. Chem. Chem. Phys.* 18 (2016) 801–810.

[65] X.Z. Li, F.B. Li, C.L. Yang, W.K. Ge, *J. Photochem. Photobiol. A* 141 (2001) 209–217.

[66] L. Yuan, Y.-J. Xu, *Appl. Surf. Sci.* 342 (2015) 154–167.

[67] L. Zhang, N. Li, H. Jiu, G. Qi, Y. Huang, *Ceram. Int.* 41 (2015) 6256–6262.